

# PROCEEDINGS OF SPIE

[SPIDigitalLibrary.org/conference-proceedings-of-spie](https://spiedigitallibrary.org/conference-proceedings-of-spie)

## Final two-stage MOAO on-sky demonstration with CANARY

E. Gendron, T. Morris, A. Basden, F. Vidal, D. Atkinson, et al.

E. Gendron, T. Morris, A. Basden, F. Vidal, D. Atkinson, U. Bitenc, T. Buey, F. Chemla, M. Cohen, C. Dickson, N. Dipper, P. Feautrier, J.-L. Gach, D. Gratadour, D. Henry, J.-M. Huet, C. Morel, S. Morris, R. Myers, J. Osborn, D. Perret, A. Reeves, G. Rousset, A. Sevin, E. Stadler, G. Talbot, S. Todd, E. Younger, "Final two-stage MOAO on-sky demonstration with CANARY," Proc. SPIE 9909, Adaptive Optics Systems V, 99090C (26 July 2016); doi: 10.1117/12.2231432

**SPIE.**

Event: SPIE Astronomical Telescopes + Instrumentation, 2016, Edinburgh, United Kingdom

# Final two-stage MOAO on-sky demonstration with CANARY

E. Gendron<sup>a</sup>, T. Morris<sup>b</sup>, A. Basden<sup>b</sup>, F. Vidal<sup>a</sup>, D. Atkinson<sup>g</sup>, U. Bitenc<sup>b</sup>, T. Buey<sup>a</sup>, F. Chemla<sup>c</sup>, M. Cohen<sup>c</sup>, C. Dickson<sup>g</sup>, N. Dipper<sup>b</sup>, P. Feautrier<sup>f,d</sup>, J-L. Gach<sup>d,e</sup>, D. Gratadour<sup>a</sup>, D. Henry<sup>g</sup>, J-M. Huet<sup>c</sup>, C. Morel<sup>a</sup>, S. Morris<sup>b</sup>, R. Myers<sup>b</sup>, J. Osborn<sup>b</sup>, D. Perret<sup>a</sup>, A. Reeves<sup>b</sup>, G. Rousset<sup>a</sup>, A. Sevin<sup>a</sup>, E. Stadler<sup>f,d</sup>, G. Talbot<sup>b</sup>, S. Todd<sup>g</sup>, E. Younger<sup>b</sup>,

<sup>a</sup> LESIA, Obs. Paris, CNRS, UPMC, Univ. Paris Diderot, 5 p. Janssen, 92190 Meudon, France

<sup>b</sup> Centre for Advanced Instrumentation, Durham Univ., South Road, Durham, DH1 3LE, UK

<sup>c</sup> GEPI, Obs. Paris, CNRS, UPMC, Univ. Paris Diderot, 5 p. Janssen, 92190 Meudon, France

<sup>d</sup> First Light Imaging S.A.S, 100 Impasse des Houillères, 13590 Meyreuil, France

<sup>e</sup> Aix Marseille Université, CNRS, LAM (Laboratoire d'Astrophysique de Marseille) UMR 7326, 13388 Marseille, France

<sup>f</sup> Institut de Planétologie et d'Astrophysique de Grenoble (UMR 5274), BP 53, 38041 Grenoble Cedex 9, France

<sup>g</sup>UKATC, Royal Observatory Edinburgh, Blackford Hill, Edinburgh, EH9 3HJ, UK

## ABSTRACT

CANARY is an on-sky Laser Guide Star (LGS) tomographic AO demonstrator in operation at the 4.2m William Herschel Telescope (WHT) in La Palma. From the early demonstration of open-loop tomography on a single deformable mirror using natural guide stars in 2010, CANARY has been progressively upgraded each year to reach its final goal in July 2015. It is now a two-stage system that mimics the future E-ELT: a GLAO-driven woofer based on 4 laser guide stars delivers a ground-layer compensated field to a figure sensor locked tweeter DM, that achieves the final on-axis tomographic compensation. We present the overall system, the control strategy and an overview of its on-sky performance.

**Keywords:** tomography, ELT, instrumentation, laser guide star, adaptive optics, wave-front sensing

## 1. INTRODUCTION

In 2007, the development programme of an on-sky demonstrator for multi-object adaptive optics (MOAO) was initiated. This took place in the framework of the pre-phase A study of the EAGLE instrument<sup>1</sup> for the European ELT, a MOAO-assisted IR spectrograph for the observation of distant galaxies. At that time, MOAO was regarded as an uncertain, challenging technique by the European community. This led the University of Durham and the Paris Observatory to propose the installation of an MOAO pathfinder called CANARY on the 4.20 m William Herschel Telescope in La Palma. The programme for setting up the full complete experiment was established through 3 main phases of increasing complexity. It started with the demonstration of open-loop tomography on natural guide stars (NGS) in 2010, where first images were successfully obtained<sup>2</sup>. Then, MOAO coupling 3 NGS and 4 Rayleigh LGS in open loop in 2013 and laser tomography AO (LTAO) in 2014 was demonstrated<sup>3</sup>. In 2015 CANARY obtained its final results, as a two-stage system that mimics the future E-ELT: a LTAO-driven woofer based on 4 LGS and 3 NGS delivers a ground-layer compensated field to a figure sensor locked tweeter DM, that achieves the final on-axis tomographic compensation. During these evolutions of CANARY, EAGLE has been merged<sup>4</sup> in 2012 with another proposal of a multi-object spectrograph to form the MOSAIC<sup>5,6</sup> instrument, for which CANARY is still the MOAO pathfinder.

CANARY has now four Rayleigh LGS wave-front sensors (WFS), three off-axis NGS WFS, two figure sensors. It also has a so-called truth sensor, that do not take part to the correction but allows us to assess the error

---

Further author information: eric.gendron at obspm.fr

breakdown, perform calibrations, and close a classical SCAO loop for reference images. The total number of slopes and actuators crunched by the real-time computer (RTC) went from  $288 \times 54$  in 2010 to  $2042 \times 297$  in 2015, a factor of 40 ahead, while the control law went from the simplest of all correctors in 2010 to a rather complex mixed LGS-NGS LTAO pseudo open-loop woofer control completed by a differential tomographic open-loop figure-locked tweeter control in 2015. All of this was accompanied by an increase of the efficiency of the instrument, from 50 to 200 files archived per night, now processed during the night as they are produced by an automated dedicated pipeline.

We will present the overall system, the control strategy and some examples of its on-sky performance, as well as some tools and techniques that were used to assess the wave-front error breakdown. The perspective for the new E-ELT project of multi object spectrograph, so-called MOSAIC, will be given.

## 2. DESCRIPTION OF THE CANARY EXPERIMENT

### 2.1 Goals, principle

CANARY is an MOAO demonstrator for the MOSAIC instrument, it is led by the University of Durham, and Paris Observatory.

CANARY is a phased experiment with three planned configurations (called A,  $B_{1/2}$ ,  $C_{1/2}$ ) that take the system from the Phase A NGS-only configuration used in 2010 through to a Phase C configuration that closely matches the proposed architecture for the MOAO on the E-ELT. Among its 5 mirrors, the E-ELT includes 2 active mirrors (M4 and M5) respectively for high-order compensation (M4, 5316 degrees of freedom) and tip-tilt (M5), that are in closed loop on all the wave-front sensors. They should provide the instrument with a global average compensation, close to a ground-layer correction. Then, the MOAO deformable mirrors, specific to each individual science channel, provide the direction-specific, tomographic compensation on top of M4-M5. This is a two-stage system, that is demonstrated by CANARY is its last phase, C2.

As a pathfinder, CANARY is simplified compared to a real system. Simplifications arise on the multiplex aspect of the instrument, which is here reduced to its very minimum: there is only a single MOAO channel, as the difficulties in MOAO do not lay in the multiplicity of the channels –this latter is a matter of engineering conception–, but rather in the open-loop control and the tomography aspects, both coming with their calibrations issues.

The instrument neither targets any particular astrophysical goal (although some successful attempts<sup>7</sup> have been achieved in 2013). The observed targets are four-star asterisms, chosen to be made of a central star observed with an IR camera, and with the 3 others off-axis, spread around the central one as regularly as possible, about 1 arc-minute away.

A particular feature of CANARY is its so-called *truth sensor*, which observes the central on-axis star synchronously with all the others wave-front sensors without taking part to the correction at all. It acts just as a spy sensor measuring the wave-front residuals in parallel to the IR science camera and allows us to diagnose the compensation performance. It also allows us to close the loop in a very standard SCAO mode, which, for us, gives the uppermost performance limit and allows to compare to the performance of all the other working modes (LTAO, MOAO, GLAO, etc). The truth sensor is also required for some numerous particular calibrations.

Last but not least, CANARY is also equipped with a telescope simulator able to provide the focal plane of the experiment with the equivalent of a stellar scene observed through the WHT. Three movable NGS can be placed anywhere in the field, with four laser beacons at selectable altitude between 13 to 20 km, all of them perturbed thanks to two rotating phase screens with Kolmogorov-like phase disturbances which altitudes can also be chosen, from 0 to 7 km. Various pupil masks, alignment beacons and alignment tools are also available, such as a rotating calibrated wedged plate (equiv. to 1" on-sky) in a pupil plane that allows us to calibrate pixel scales for the whole experiment.

Table 1 summarises the phases CANARY went through over the past 5 years of on-sky operation. It has regularly been enriched with new capabilities over the years. This progressive transformation had been programmed at the origin, and made possible thanks to the modularity of its optical setup. A detailed history of the system evolution is given by Basden et al.<sup>8</sup>. Year 2014 made a remarkable break in the evolution, as this was a pure

Phase	Year	Nb NGS SH size Camera	Nb LGS SH size Camera	Truth sensor	Woofers loop Nb actus	Tweeter loop Nb actus	Figure sensor loop	Tomography
A	2010	3 $7 \times 7$ Andor 128 <sup>2</sup>		$7 \times 7$	open 52	0		yes NGS
B1	2012	3 $7 \times 7$ Andor 128 <sup>2</sup>	1 $7 \times 7$ Andor 128 <sup>2</sup>	$7 \times 7$	open 52	0		yes LGS+NGS
B2	2013	3 $7 \times 7$ Andor 128 <sup>2</sup>	4 $7 \times 7$ Scimeasure	$7 \times 7$	open 52	0		yes LGS+NGS
C1	2014	3 $7 \times 7$ Andor 128 <sup>2</sup>	4 $7 \times 7$ Scimeasure / OCAM	$7 \times 7$	closed LTAO 52	0	on woofer	yes LGS+NGS
C2	2015	3 $7 \times 7$ Andor 128 <sup>2</sup>	4 $14 \times 14$ OCAM	$14 \times 14$	closed LTAO 52	open / fig-locked 241	on tweeter	yes LGS+NGS
D	2016	2 $7 \times 7$ Andor 128 <sup>2</sup>	1 (sodium) $7 \times 7$ OCAM	$7 \times 7$	LTAO			

Table 1. CANARY has been upgraded over the years, and has passed across phases of increasing complexity. Only the NGS wave-front sensors have remained the same across phases. The LGS wave-front sensors went from a single, on-axis beacon to four off-axis ones sensed with high-orders  $14 \times 14$  sensors. The woofer has 52 actuators plus 2 tip-tilt axis, and was the only deformable mirror until 2015. Before end of 2013, the control was applied in full open-loop on the woofer deformable mirror. In 2014, an important break occurred in the philosophy of the instrument, as the woofer turned to closed-loop control, so that 2014 became a LTAO-year. This operation was required to prepare the final 2-stage set-up of 2015, and was made possible thanks to the optical modularity of the experiment. In 2015, the addition of a tweeter with 241 actuators allowed us to reach the complete E-ELT simulation setup.

LTAO phase, instead of MOAO. This transition phase was however required to prepare the last step: the 2-stage set up of the E-ELT, where the telescope adaptive mirror called M4 is in closed-loop with all the wave-front sensors, while the MOAO deformable mirror is still of course in open-loop behind the woofer. This was required to gain in experience with the LTAO setup, and its new control law, before entering the last 2-stage phase.

### 3. TECHNICAL DESCRIPTION

#### 3.1 NGS wave-front sensors

The NGS wave-front sensors use Andor iXonEM 860 EMCCD cameras with  $24 \mu\text{m}$  pixel size, featuring  $128 \times 128$  pixels, and we use  $16 \times 16$  pixels per sub-aperture of respectively  $0.283''$ ,  $0.260''$  and  $0.285''$  for the 3 wave-front sensors. The total field of view is about 4.5 arcsec, that allows us to accommodate for the open-loop requirements. The full array is read, however the centroiding zone may be chosen by the real-time computer smaller than the full  $16 \times 16$  area in order to reduce the impact of noise. These cameras are electron-multiplied CCDs, and feature a read-out noise of 0.5 electron rms per pixel. The three NGS wave-front sensors can be positioned anywhere within a 2.5 arcmin field of view in diameter. They all have  $7 \times 7$  sub-apertures. With a telescope central obscuration of diameter of 28.5% of that of the pupil, the 4 central sub-apertures are under-illuminated by a factor close to 0.5.

#### 3.2 Truth sensor

The *truth sensor* is also based on the same Andor iXonEM 860 EMCCD camera than the NGS ones, but here the Hartmann is  $14 \times 14$  sub-apertures, with  $8 \times 8$  pixels of  $0.491''$ . The rather coarse sampling here has been

chosen in order to get a sufficient field of view of 3.9" per sub-aperture. The truth sensor is fixed, at the centre of the field of view.

### 3.3 Lasers

The laser is of Rayleigh type at 532 nm (green) with a measured power of 28W. It is pulsed at a 10 kHz rate. The 4-LGS asterism is created by inserting a diffractive optical element (DOE) into the existing GLAS laser launch system. The DOE is mounted in a rotation stage to compensate for field de-rotation at the WHT Nasmyth platform. The laser beacons are located on the corners of a square, 23" away from the centre of the field. The laser clock is the master clock that synchronises the rest of the system (i.e. all the cameras). The laser altitude was set to 14 km for the phase C2.

### 3.4 LGS wave-front sensors

At the focal plane after the first optical relay, a 532 nm rugate notch filter sends the laser light towards the LGS wave-front sensor path. This latter contains a fast steering mirror for the correction of LGS launch jitter capable of  $\pm 4''$  of on-sky motion at bandwidths of up to 150Hz. This tip-tilt mirror is in a pupil plane common to each of the LGS, so can only remove tip-tilt motion caused by telescope vibration and ground layer turbulence.

The four focusing beams from the 4 lasers are made telecentric in the wave-front sensor (pupil at infinity), and they are deviated before the focal plane using a pyramid-shaped prism placed at a convenient location. This pyramid provides the right angle both to properly separate the pupils from each beam, and make the four beacons to exactly overlap onto the same field stop, square, 7" wide. This setup allows us to get the four Hartmannograms on the same array of micro-lenses, and same detector.

In phase C2, the detector is a gated, electron-multiplied OCAM2S camera<sup>9</sup> from LAM, using E2V's CCD219 sensor with integral shutter and featuring a read-out noise better than 0.5 electron per pixel. Pixel size is 24  $\mu\text{m}$ . We have  $8 \times 8$  pixels per microlens, and  $14 \times 14$  sub-apertures in each of the 4 wave-front sensors. The on-sky pixel size is measured to be, for the 4 wave-front sensors, 0.851", 0.864", 0.859", 0.871".

### 3.5 Woofer deformable mirror

The deformable mirror is of piezostack type, built by CILAS in 1990. It has  $8 \times 8$  actuators with a pitch of 9.5 mm, and a coupling (*coupling*: value of the influence function of an actuator normalised to peak value, taken at the location of the nearest neighbour) of the order of 0.25. The surface at rest is measured to be of the order of 250 nm rms (mostly cylinder), and the best flat is unfortunately 120 nm rms due to some inter-actuator high spatial frequencies. These latter come from the fact that this mirror had previously been used for more than 10 years by ESO on the ADONIS AO system at the 3.6m telescope in La Silla Observatory from 1992 to 2004. The mirror is made in a hard piezoelectric material in order to dissipate less power and minimize hysteresis effect ; for this reason the mirror has been measured<sup>10</sup> to have an hysteresis below 2%, and the open-loop characteristics allow us to obtain an excellent go-to error of 3 to 4% of the rms commanded wavefront. This allowed us to use this deformable mirror in a full open-loop fashion in the phases A and B of the CANARY project.

The tip-tilt mirror is a copy of that used in Saxo,<sup>11</sup> the VLT AO of the SPHERE instrument. Its position is servo-controlled by internal sensors so that it has virtually no go-to error.

### 3.6 Tweeter deformable mirror

The tweeter deformable mirror is of a magnetic (voice-coil) type. It is a Hi-Speed-DM241-25 from the ALPAO SaS company, which has 241 useful actuators in a  $17 \times 17$  array with an actuator pitch of 2.5 mm, a coupling of the order of 0.50. The useful pupil diameter was chosen to 37.5 mm (first and last row/columns of actuators are located out of the pupil by half the actuator pitch). An overview of these magnetic devices are detailed by Charton et al.<sup>12</sup>. The mirror has an excellent linear response, but suffers from a slight creeping effect that makes the mirror drifting when a static voltage is applied. The open-loop properties of this mirror have been studied by Bitenc et al.<sup>13</sup> who proposes a feed-forward compensation scheme for this creeping effect. Unfortunately this only applies to long-term drifts, while our measurements show that the creeping is present at any timescales. A typical increase of +2% on the amplitude of the measured wavefront is measured 0.1 s after the application of

the command, then +2% again after 1 s, then +2% after 10s, and so on every decade. This is indeed typical of a creeping effect, known to behave as  $z(t) = z(t_0)(1 + g \ln(t/t_0))$ .

For this reason, a figure sensor has been added to that mirror. It is a  $14 \times 14$  sub-aperture Shack-Hartmann, with  $10 \times 10$  pixels per sub-aperture, a pixel scale of  $0.614''$  per pixel. This sensor is located at the very edge of the field of view (1.3 arc-minutes off-axis), and is looking at an on-bench source with a diameter of  $\approx 2$  pixels. The light path, between the source and the sensor, sees only the tweeter deformable mirror, with the 2 off-axis parabolae and 2 plane mirrors that form the optical relay.

### 3.7 IR camera

The Camicaz camera<sup>14</sup> is the IR science camera of CANARY. It is a  $256 \times 256$  HgCdTe NICMOS3 detector, cooled down to  $77^\circ\text{K}$  using a liquid nitrogen cryostat. It includes a cold pupil stop and a filter wheel with 8 positions with standard J, H and Ks filters, a series of narrow-band filters and a dark position. It also includes a pupil imaging lens, the main application of which being the alignment of the cold stop with the CANARY pupil. The pixel scale is 30.8 mas per pixel, corresponding to Nyquist sampling at  $\lambda = 1.25\mu\text{m}$ . H and K bands are thus (slightly) oversampled. The camera read-out noise is 25 electrons rms per pixel.

### 3.8 Real-time computer

Real-time control for CANARY is provided by the Durham AO Real-time Controller (DARC)<sup>15</sup>. This is a high performance, flexible CPU based system, which is open source. For CANARY, using moderate hardware, a latency smaller than  $700 \mu\text{s}$  is achieved, defined between readout of last WFS pixel and setting of last DM actuator. The flexibility afforded by DARC allows many different algorithms to be selected on-the-fly, or even developed without stopping the real-time system. Algorithms tested on-sky include command laws for open and closed loop operation, figure sensor operation, LQG control<sup>16</sup>, GPU powered wavefront reconstruction, and a variety of centring algorithms (namely brightest pixel selection providing an adaptive window on a per-subaperture basis<sup>17</sup>, correlation, weighted centre of gravity centring, all of them possibly used in conjunction with an adaptive windowing (spot tracking) allowing sub-apertures to be sub-windowed to reduce the effect of readout noise). A powerful telemetry system allows pixel and slope data to be recorded at full rate, while simultaneously viewing real-time displays of the data. DARC proved to be highly stable and reliable during operation, essential for any on-sky experiment.

## 4. DESCRIPTION OF THE CONTROL SCHEME

All the notations in this section are summarised in Table 2. Phases A and B were controlling the deformable mirror in full a open-loop way, which made the control law rather straightforward. The control law was

$$w_k = (1 - g) w_{k-1} - g G_s^w s_k \quad (1)$$

where  $w_k$  is the DM command,  $s_k$  the measurement vector of all the WFS (here in open loop), and  $G_s^w$  the command matrix, product of tomographic reconstructor and command matrix of the truth sensor. The factor  $g$  is the gain, used for filtering out some noise at high temporal frequencies (smoothing the signal).

### 4.1 Pseudo open-loop control for the woofer

With phase C, wave-front sensors become in closed-loop and see the action of the woofer deformable mirror. The idea is to use Eq. 1, feeding it with the pseudo open-loop measurement  $s(k)$  computed from the closed-loop measurement  $y(k)$  of all wave-front sensors using

$$s_k = y_k - D_w^y((1 - a) w_{k-1} + a w_{k-2}) \quad (2)$$

where  $D_w^y$  is the overall interaction matrix of the woofer with all wave-front sensors, and the parameter  $a$  is the number of frames of latency between the end of the integration of the wave-front sensor and the start of command application on the DM. We have tested this command law in phase C1 in 2014 using  $a = 0.3$  and noticed that we could simplify it and use  $a = 0$  with no significant change in the performance. For this reason,

variable	meaning
$w_k$	voltage vector on woofer at frame $k$
$v_k$	voltage vector on the tweeter at frame $k$
$V_k$	global voltage vector for the 2 mirrors, that concatenates $v_k$ and $w_k$
$y_k$	measurement vector, as seen by the on-sky off-axis WFSs, at frame $k$
$s_k$	measurement vector the on-sky off-axis WFS would have produced if loop had not been engaged, at frame $k$ (i.e. pseudo-open-loop measurement)
$f_k$	measurement vector of the figure sensor of the tweeter at frame $k$
$Y_k$	global measurement vector that concatenates $y_k$ followed by $f_k$
$D_w^y$	interaction matrix woofer $\rightarrow$ measurements of on-sky off-axis WFSs
$G_s^w$	control matrix from measurements of on-sky off-axis WFSs $\rightarrow$ woofer (GLAO command)
$R$	tomographic reconstructor
$D_w^{ts}$	interaction matrix woofer $\rightarrow$ truth sensor
$D_t^{ts}$	interaction matrix tweeter $\rightarrow$ truth sensor
$D_t^{ts\dagger}$	command matrix truth sensor $\rightarrow$ tweeter
$R$	tomographic reconstructor for the tweeter (open-loop off-axis slopes $\rightarrow$ tweeter voltages, Eq. 15)
$R'$	tomographic reconstructor for the truth sensor (open-loop off-axis slopes $\rightarrow$ truth sensor, Eq. 14)

Table 2. Summary of notations.

and for the sake of simplicity in the equations of this article, we will use  $a = 0$  in the following. Replacing Eq. 2 into Eq. 1 leads to the control law for the woofer:

$$w_k = (1 - g + gG_s^w D_w^y) w_{k-1} - gG_s^w y_k. \quad (3)$$

The reconstructor  $G_s^w$  may be of any type. In phase C1 (LTAO),  $G_s^w$  was a tomographic reconstructor optimised for the best possible on-axis compensation. In phase C2 (2-stage MOAO),  $G_s^w$  should rather be a GLAO-like reconstructor if we want to mimic the E-ELT situation, and more detailed explanations will be given in Sect. 6.4. Whatever the case, the control law is still the same.

## 4.2 Tweeter control

MOSAIC will have several MOAO deformable mirrors. We made the assumption that that the control of the woofer M4 should be totally independent from what is happening in the MOAO channels. If the shape of M4 was dependent, or coupled to that of the tweeter, the situation would be “impossible” to manage with 20 tweeters in parallel as in EAGLE or MOSAIC, creating a situation of global coupling between all the adaptive mirrors. For this reason, we assume that whatever the MOAO-tweeter DMs are doing, there will be no feedback of their action towards M4/woofer.

### 4.2.1 Pure open loop case

Consequently, each tweeter is required to complement the action of the woofer in order to perform the right tomographic compensation along its observing direction. This requires to establish a relation between tweeter and woofer: the action of the woofer should not be compensated twice and the woofer command should be turned into a command to the tweeter, to be subtracted from this latter. We will use the truth sensor for this on-bench calibration. The interaction matrices on the truth sensor, both of the woofer and the tweeter, allows us to link those two mirrors and transform a command  $w_k$  into the equivalent command on the tweeter  $v_k = D_t^{ts\dagger} D_w^{ts} w_k$ . Then, the command law for the open-loop tweeter commands can be written as

$$v_k = (1 - g')v_{k-1} - g'R s_k - g'D_t^{ts\dagger} D_w^{ts} w_k \quad (4)$$

where we recall that  $s_k$  are the (pseudo) open-loop slopes computed following Eq. 2, that needs to be replaced in the previous equation, as well as the value of  $w_k$  that should be replaced according to Eq. 3 to get an expression only depending on terms from the frame  $k - 1$  :

$$v_k = (1 - g')v_{k-1} + g'[R D_w^y - D_t^{ts\dagger} D_w^{ts} (1 - g + gG_s^w D_w^y)] w_{k-1} + g'[D_t^{ts\dagger} D_w^{ts} gG_s^w - R] y_k \quad (5)$$

This command law, complex at first sight, become much more friendly when coupled to Eq. 3 and displayed as

$$V_k = A V_{k-1} + B Y_k \quad (6)$$

with  $A$  and  $B$  some matrices with their blocks properly filled as follows :

$$A = \begin{bmatrix} 1 - g + gG_s^w D_w^y & 0 \\ [g'R D_w^y - g'D_t^{ts\dagger} D_w^{ts} (1 - g + gG_s^w D_w^y)] & (1 - g') \end{bmatrix} \text{ and } B = \begin{bmatrix} -gG_s^w & 0 \\ g'D_t^{ts\dagger} D_w^{ts} gG_s^w - g'R & 0 \end{bmatrix} . \quad (7)$$

#### 4.2.2 Figure-locked mode

In this mode, we are using the figure sensor on the tweeter in order to measure and control its shape to avoid any go-to error. The strategy is to make a main classical SCAO loop on the tweeter, driven by the figure sensor, and using an integral controller with gain  $g'$ . This can be written as

$$v_k = v_{k-1} - g'D_t^{f\dagger} (f_k - f_k^{setpoint}) \quad (8)$$

with  $f_k$  the measurement vector of the figure sensor on the tweeter. This loop is known to bring the tweeter to a shape measured as  $f_k^{setpoint}$  by the figure sensor. Our strategy is then to set at each frame a new  $f_k^{setpoint}$ , according to what the tweeter should do. We can then write that the setpoint should be the tomographic command, subtracted from the shape of the woofer translated into a tweeter command (as we already did in Eq. 4), or

$$f_k^{setpoint} = -D_t^f R s_k - D_t^f D_t^{ts\dagger} D_w^{ts} w_k \quad (9)$$

In this equation we now need to replace  $s_k$  using Eq. 2,  $w_k$  using Eq. 3, and replace Eq. 9 into Eq. 8. We find that,

$$v_k = v_{k-1} - g'D_t^{f\dagger} f_k + g'D_t^{f\dagger} [D_t^f D_t^{ts\dagger} D_w^{ts} gG_s^w - D_t^f R] y_k + g'D_t^{f\dagger} [D_t^f R D_w^y - D_t^f D_t^{ts\dagger} D_w^{ts} (1 - g + gG_s^w D_w^y)] w_{k-1} \quad (10)$$

that rewrites

$$V_k = A V_{k-1} + B Y_k \quad (11)$$

with the block matrices  $A$  and  $B$  defined as

$$A = \begin{bmatrix} 1 - g + gG_s^w D_w^y & 0 \\ g'D_t^{f\dagger} [D_t^f R D_w^y - D_t^f D_t^{ts\dagger} D_w^{ts} (1 - g + gG_s^w D_w^y)] & 1 \end{bmatrix} \quad (12)$$

$$B = \begin{bmatrix} -gG_s^w & 0 \\ g'D_t^{f\dagger} [D_t^f D_t^{ts\dagger} D_w^{ts} gG_s^w - D_t^f R] & -g'D_t^{f\dagger} \end{bmatrix} . \quad (13)$$

## 5. TOMOGRAPHY

As suggested in the previous section, the tomographic reconstructor  $R$  is applied on pseudo open-loop data. Therefore, it is built and optimised for open-loop data, in a way strictly similar to the previous open-loop phases A and B of CANARY. It is a measurement-based MMSE (minimum mean square error) reconstructor. This means that it linearly combines off-axis slopes measurements to find the best estimation of the *measurements* that would be obtained on-axis (instead of wavefront, or Zernike modes, or KL modes, or phase as usual). This can be written as

$$R' = C_{tm} \cdot C_{mm}^{-1} \quad (14)$$

with  $C_{tm}$  the covariance matrix between the ideal measurements that would be done on-axis, and the off-axis measurements.  $C_{mm}$  is the covariance matrix between off-axis measurements ; it includes the measurement noise on its diagonal. The final tomographic reconstructor  $R$ , as it appears in Eq. 4, is computed using

$$R = D_t^{ts\dagger} R' \quad (15)$$

in order to get volts on output. This step, from on-axis slopes to DM voltages is known to be sub-optimal in our approach. However, this offers the huge advantage of being calibrated experimentally, which is the specific and very important point that justifies the particular choice of this approach.

The management of the lasers, coming with their indetermination problem on the tilt (and possibly defocus), is taken into account in the Eq. 14. We have chosen a global approach for that, as opposed to techniques known as split tomography<sup>18</sup> where the reconstruction is performed independently for LGS and NGS. The matrix  $C_{mm}$  is reworked before applying Eq. 14: it has been multiplied on its left and right-hand sides by a tilt-filtering matrix on the laser wave-front sensors. After filtering, the covariance matrix  $C_{mm}$  should be understood as the covariance of measurements deprived from the undetermined modes. The inversion process then makes some null eigenvalues to appear, corresponding to the filtered undetermined modes, and that will in return be filtered out from the command. Another method used by Tallon et al.<sup>19</sup> can also be applied, that consists in modifying the diagonal LGS wave-front sensor blocks of the covariance matrix by adding them a covariance matrix of undetermined modes measurements, with a large amplitude. This is like adding a noise on the measured undetermined modes, that will automatically result in their filtering by the inversion process.

## 5.1 Learn & Apply

The expression 14 is purely theoretical, it is obtained by solving  $R'$  that minimises the quantity  $\langle |t - R'm|^2 \rangle$ . It has been noted very soon that, because CANARY is equipped with a truth sensor performing on-axis measurements, both matrices  $C_{tm}$  and  $C_{mm}$  could be *measured* on-sky from open-loop data (which would be cheating, as no real MOAO instrument would have an on-sky truth sensor). At the opposite, a real MOAO instrument should generate the matrices  $C_{tm}$  and  $C_{mm}$  from a model, based on the knowledge of the instrument (number of sub-apertures, registration of WFS, pointing directions of WFSs, noise on measurements, sensitivity (pixel scale) of each WFS, etc) and atmospheric  $C_n^2(h)$  profile and outer scale  $L_0$ . However, those two points of view are not so antagonist, as the matrix  $C_{mm}$  can still be measured on-sky anyway, and compared to the model : this was the idea at the origin of the *Learn & Apply* algorithm.

*Learn & Apply* is the name of a method that consists in estimating the parameters of the instrument/atmosphere model, by fitting the modelled  $C_{mm}$  matrix to the observed one. The goal is to produce a covariance matrix that best fits the observed data, in order to produce the tomographic reconstructor. A nice by-product is the set of fitted parameters, that brings some information about the atmospheric profile.

The procedure minimising the distance between the modelled covariance matrix and the experimental one is based on a Levenberg-Marquardt algorithm. This is an iterative procedure, that requires to be able to recompute frequently the covariance matrix. Let  $n$  be the number of parameters to be fitted ; each iteration requires  $n + 1$  computations, and an average number of 10 iterations is required so that  $\approx 100 - 200$  matrix compute are required. Early computations used a Fourier-based model<sup>20,21</sup> to get the bi-dimensional (2D) spatial covariance of the wave-front slopes. We have now developed a method that allows us to compute each coefficient of the matrix independently<sup>22,23</sup> , which is a great advantage for faster computation when considering a parallel implementation<sup>23</sup> , now performed using GPUs (graphics processing units). With matrices  $1656 \times 1656$ , the *L&A* procedure now takes less than 30 seconds on CANARY.

## 5.2 Sensitivity to profile variations: the VED

Once the tomographic reconstructor is known, and that we also know the matrices  $C_{mm}$ ,  $C_{tm}$  and  $C_{tt}$ , computing the covariance matrix of the tomographic error is given by

$$C_{ee} = C_{tt} - C_{tm}R'^t - R'C_{tm}^t + R'C_{mm}R'^t \quad (16)$$

This equation could be simplified when considering Eq. 14, but we should avoid that if we want to keep it general for any arbitrary  $R'$ . The tomographic error, expressed as a wavefront error, is then derived from  $C_{ee}$  by projecting/reconstructing onto any suitable modal basis  $P$  to get  $\sigma_{tomo}^2 = \text{Trace}(P.C_{ee}.P^t)$ .

The turbulence profile is known to evolve with time, each layer being subject to variations both in strength and in altitude. How does Eq. 16 modifies with these changes ? All the covariance matrices are modified with profile variations, while  $R'$  is kept fixed. Our idea is that Eq. 16 is linear<sup>24</sup> with respect to  $C_n^2(h)$ , because

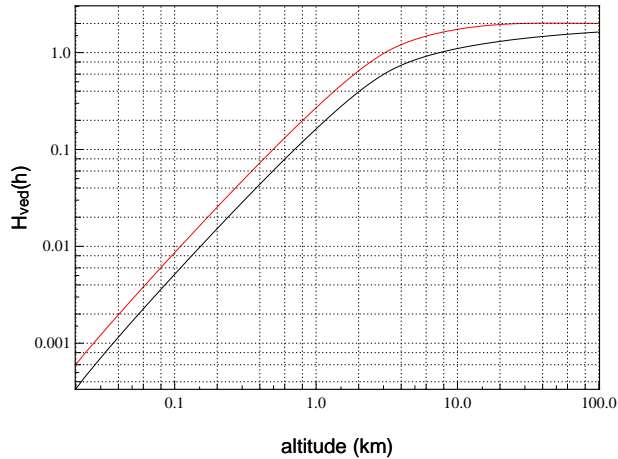


Figure 1. Transfer function  $H_{VED}$  of a SCAO system locked on an off-axis star. Here the VED shows how the anisoplanatic error grows with altitude of the layer. The slope of the function at small altitudes is in  $h^{\frac{5}{3}}$ . At  $h \rightarrow \infty$  the function tends asymptotically towards 2, as the on- and off-axis wavefronts become uncorrelated. Black lower plot is for  $L_0 = \infty$ , the upper red one has  $L_0 = 25$  m.

individual layers produce independent stochastic phenomenon, so that the total covariance matrix of the full atmosphere is the sum of the matrices associated to each individual layer: they just add up together to form the total one. Therefore, a tomographic error can be computed for each individual layer, and the total forms the full tomographic error.

$$\sigma_{tomo}^2 = \sum_{l=1}^L \sigma_{tomo}^2(h_l) \quad (17)$$

Let now  $\sigma^2(h)$  be the variance of a single layer at altitude  $h$  per unit of  $h$ . Let us define  $H_{VED}(h)$ , the ratio between the tomographic error variance and the layer variance, both taken at same altitude  $h$ :

$$H_{VED}(R', h) = \frac{\sigma_{tomo}^2(h)}{\sigma^2(h)} \quad (18)$$

It comes

$$\sigma_{tomo}^2 = \int H_{VED}(R', h) \sigma^2(h) dh \quad (19)$$

The  $H_{VED}(R', h)$  is the vertical error distribution (VED) transfer function associated to the reconstructor  $R'$ . We call it a transfer function based on the similarity with the transfer function of any linear filtering process, where the output variance is determined from an input power spectral density  $\epsilon^2(\nu)$  using  $\int H(\nu) \epsilon^2(\nu) d\nu$ ; but here frequency has been turned into altitude, and power spectral density into  $C_n^2(h)$  profile. The observation of the VED curve tells us a lot on how turbulent layers are rejected, and on the sensitivity to changes in  $C_n^2(h)$ .

### 5.2.1 The trivial SCAO example

Let us assume a system on a 4.2 m telescope with a single wave-front sensor performing SCAO on a 40" off-axis star, with a tomographic reconstructor  $R' = \text{Identity}$  for estimating the on-axis slopes on  $7 \times 7$  Shack-Hartmann. Let us define the tomographic error as  $\sigma_{tomo}^2 = \text{Trace}(C_{ee})$ , the residual variance of the Shack-Hartmann slopes. We expect the anisoplanatic error –expressed on slopes– to be the tomographic error. Computing  $H_{VED}$  for an Id matrix is given on Fig. 1, where we can see that the error first grows as  $h^{\frac{5}{3}}$  before tending towards 2 for infinitely large altitudes, where wavefronts become uncorrelated. Of course we have  $H_{VED}(0) = 0$ , as perturbations in the pupil plane are ideally compensated, regardless of the guide star field direction.

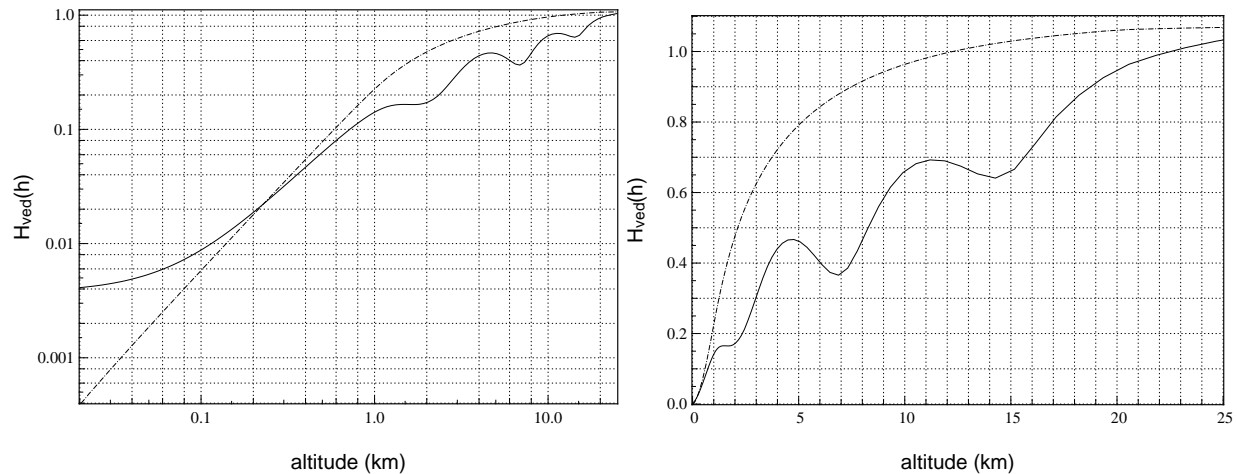


Figure 2. Plain line: Transfer function  $H_{VED}$  of a CANARY tomographic reconstructor with 4 lasers 23" off-axis and 3 NGS, 150 nm noise, 4 layers at [0,2,7,15] km of strength [0.8,0.1,0.05,0.05],  $L_0 = 25$  m. Dashed line: Transfer function  $H_{VED}$  of a GLAO reconstructor for the same star configuration. The two graphs are identical: left one is a log-scale.

### 5.2.2 CANARY examples

We consider 4 laser guide stars 23" off-axis on a square, and 3 natural guide stars. The noise is 150 nm rms on each wave-front sensors. We consider a 4-layer profile of normalised strengths (0.8, 0.1, 0.05, 0.05) at (0, 2, 7, 15) km. The outer scale is 25 m. The VED computed in this case is shown on Fig. 2 respectively in log- and linear scale on left and right. It is also compared with the VED of a GLAO reconstructor (dashed line). The notch rejection holes are clearly visible at the locations of layers for which the reconstructor has been optimised, while the GLAO is monotonic.

The tomographic reconstructor allows to gain a factor of typically  $\approx 2$  on the altitude layers compared to GLAO, at the expense of the rejection factor at  $h = 0$ . This is a general behaviour of MMSE reconstructors. Firstly, the rejection factor at  $h = 0$  is never equal to 0 ; as any other layer, the ground layer is only partly compensated. Secondly, the rejection factor cannot be improved somewhere, without being relaxed at other altitudes (somewhat similar to the known "waterbed effect" of transfer functions in control theory).

The width of the "notch holes" is of the order of 1 to 2 km, which means that the altitude of the layers does not need to be determined to an accuracy better than 1 km, and that its altitude may vary by the same amount without any damage to the compensation.

When the relative amplitude of layers varies in time, the reconstructor  $R'$  is not adapted any more. However, the VED tells us this is not dramatic, as the rejection holes are still present at the layer locations.

## 6. ON-SKY RESULTS

### 6.1 Observing runs, asterisms

The observing nights in 2015 were 6 nights on 26, 27, 28, 29, 30 of June and 1st of July for the first run, then 6 other nights on 29, 30 Sept, 1, 3, 4, 5 Oct. Only 8 of them can be exploited, 4 of them being lost due mostly to weather conditions, and partly technical issues. The summary of the nights, together with the observed asterisms, are shown in Table 3. Many asterisms were only using 2 natural guide stars, as shown on Fig. 3.

### 6.2 Statistical results

The Fig. 4 shows part of the set of measurements (656 points, H-band SR versus seeing at 500 nm) that have been obtained in 2015. This figure combines the points from different asterisms, obtained on different nights and for different system configurations.

Night	Observed asterisms	Remarks	
June	26	A34, A47	
	27	ASTT1, A34, A47	
	28	A34, A47	
	29	ASTT1, A34, A47	bad seeing ( $> 2.5''$ during 4 hours)
	30	ASTT1, A34, A47	poor seeing before midnight
July	1	ASTT1, A34, A47	
Sept.	29	C88, A396	
	30	A53, A396	many technical issues
Oct.	1	C69, A53, C88	night lost (seeing, humidity)
	3		night lost (bad weather)
	4		night lost (weather, humidity & seeing $\geq 3''$ )
	5	C69, C88	

Table 3. A total of 12 nights were allocated to CANARY in 2015 for the final C2 phase. Among them, 8 nights only can actually be exploited.

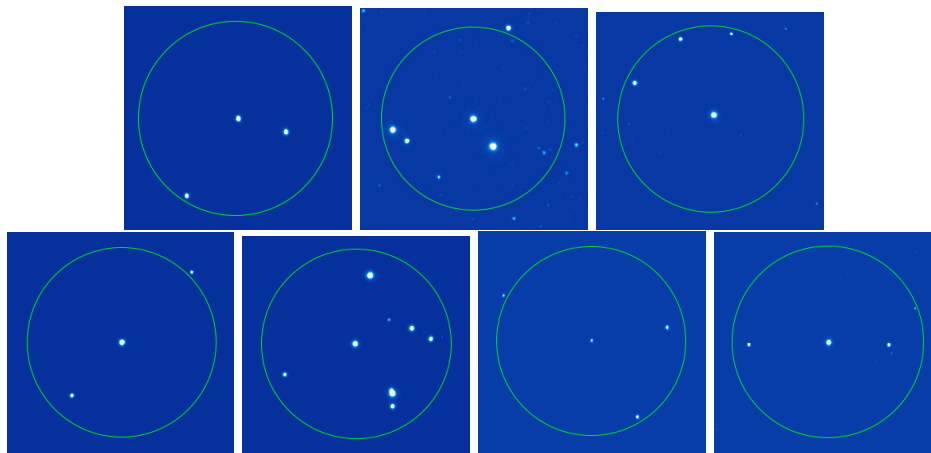


Figure 3. CANARY asterisms, as seen by the acquisition camera. Up: “July” targets ASTT1, A34, A47. Down: “October” targets C88, A396, A53, C69. The circle is 2 arcmin diameter.

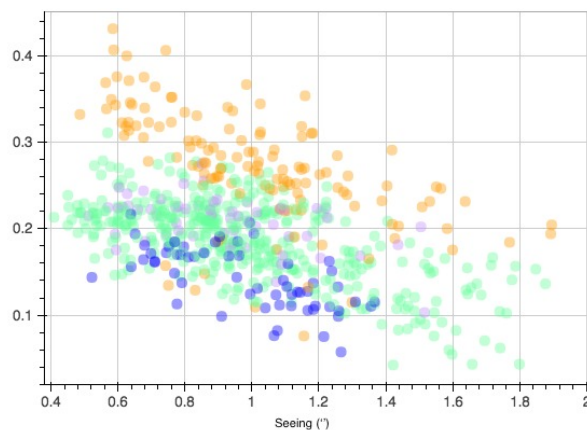


Figure 4. Set of measurements (SR in H band versus seeing) obtained with CANARY in 2015. Orange: SCAO. Dark blue: GLAO in woofer-tweeter mode. Green: woofer-tweeter MOAO by tomography.

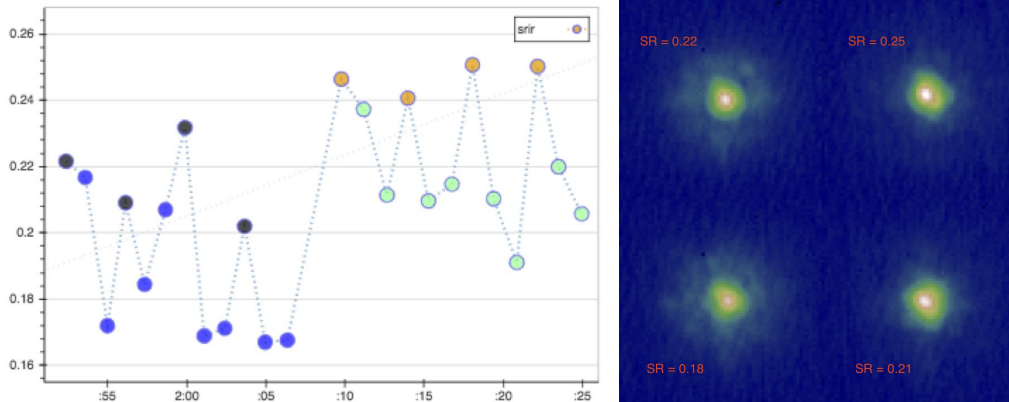


Figure 5. : **Graph:** Strehl ratio measured on the IR camera, as a function of time. Four different modes are explored. Left part: only the woofer DM is active. Right part: both woofer and tweeter are active. In each part, the upper points are SCAO, the lower ones are tomographic modes. : **Images:** PSF corresponding to the script. Left images: woofer only. Right images: woofer and tweeter. Up: SCAO. Down: tomographic modes.

It exhibits a large dispersion, while plotted against seeing value. Although uncomfortable for the eye, this dispersion is real. Part of it comes from the combination of measurements done on different asterisms, obtained on different nights, with stars of different magnitudes. Another part comes from the variation of the speed to turbulence. For tomographic points, another part is due to variations of the profile and the change of tomographic reconstructor. Another part comes from the different tests we have performed, leading to performance variations. Finally a last part is inherent to the adaptive optics, or imaging through turbulence: each IR image is obtained using a total integration time of 30 seconds, and is a particular random draw which characteristics are not entirely determined by a single number (the seeing value).

However, the purpose of this graph is first to show the impressive amount of data that could be obtained with CANARY, but also to show how MOAO compares to SCAO and GLAO, on average, at the WHT site. Taken at a seeing of 1", the GLAO-MOAO-SCAO respectively perform at H-Strehl levels of 0.15, 0.20, and 0.30. Although interesting for statistic information, this does not say much about the system performance in a given particular case.

Getting a precise information about the system performance, and comparing it between different modes (GLAO, MOAO, SCAO) requires a rather long integration time, of the order of 2 to 3 minutes in order to properly average the image. Unfortunately, 3 minutes is enough to get turbulence variations that make the comparison with the next measurements void. Our strategy is to produce images of 2 minutes integration, split into 4 images of 30 seconds, one every 2 minutes. During the time between exposures, another AO mode is tested using the same strategy. The sequence is thus A-b-c-A-b-c-A-b-c-... The sequence of a given type of images all sample the same large time interval of the order of 10 minutes and the SR can be averaged per AO mode. We call this sequence a script. Only scripts can really show the difference between AO modes, as the interleaving really averages turbulence conditions over the same period of time.

### 6.3 Script example 1

We present an example of two consecutive scripts (scripts 45 and 46, night of July 1<sup>st</sup> 2015, 01:52 to 2:24), which results (SR in H band) is shown versus time on Fig. 5. The scripts repeat the sequence [A-b-b] four times, the modes A and b are described in the table below (together with the Strehl ratio measured on-sky) :

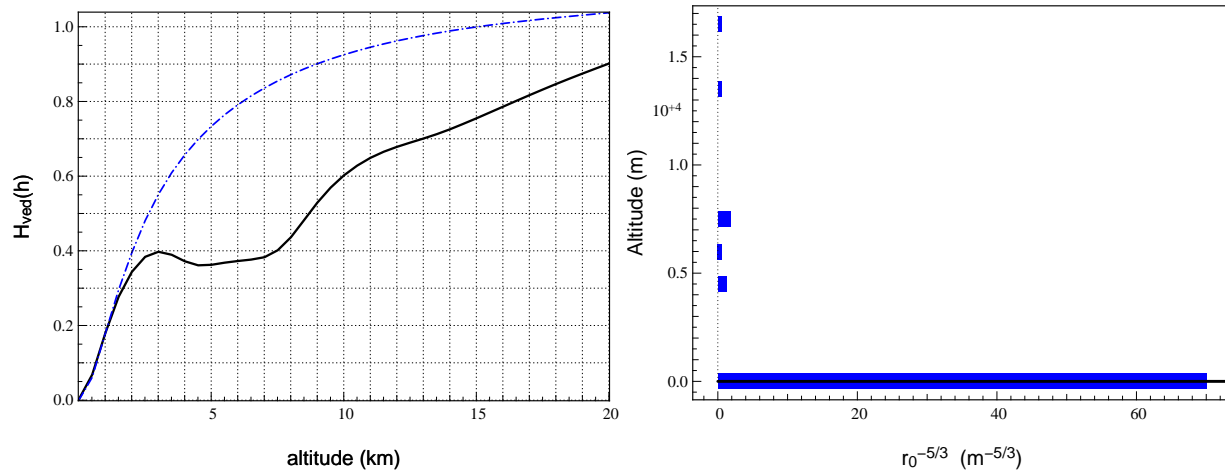


Figure 6. Left: VED transfer function for the profile shown on the right (plain line) compared to GLAO (dashed blue line). The value of the VED at  $h = 0$  is 0.003. Right: Profile that was used for the tomographic reconstructor for the scripts shown on Fig. 5.

AO mode	Script 1		Script 2	
A	woofer	SCAO	woofer	SCAO
	tweeter	–	tweeter	SCAO
	SR = 22%		SR = 25%	
b	woofer	LTAO	woofer	GLAO
	tweeter	–	tweeter	MOAO
	SR = 18%		SR = 21%	

Script 1 is using the woofer alone. Script 2 uses both mirrors. The comparison of scripts 1 and 2 shows the improvement due to the use of the tweeter. In each case, 3 to 4 points in SR are gained when using the tweeter. The comparison between modes A and b allow to see the “distance” to SCAO, and in each case the SCAO is 4 points above off-axis modes.

The  $C_n^2(h)$  profile was, as often, dominated by a ground layer (0–500 m) with a fraction of 0.93 of the total energy, 0.05 distributed from 4000 to 7000m, and the 0.02 left around 15 km. This profile is shown on Fig. 6. The VED transfer function is presented the left of Fig. 6 and shows that even a faint altitude layers have a strong impact on the VED and attenuates by a factor of 2 the impact of layers at 4–7 km compared to GLAO.

## 6.4 Script example 2

This scripts 36 and 37 (night of June 27 2015, 02:00 to 02:45) compares the loop performance when using different woofer controls. We have -at least- 5 different reconstructors, i.e. 5 ways of controlling the woofer. The reconstructor can be

<b>TOMO</b>	tomographic, on-axis reconstructor for the woofer
<b>GLAO–mean</b>	glao by averaging the wavefronts from all the wave-front sensors
<b>GLAO–ls</b>	glao by least-square fitting of data of all off-axis wave-front sensors
<b>GLAO–ground</b>	glao from tomographic reconstruction, assuming the profile is just made by a ground layer
<b>GLAO–tomo</b>	tomographic glao where profile is known and only the ground layer is reconstructed.

In this script we have compared the performance of the loop when using TOMO, GLAO–mean, GLAO–ls on the woofer. The results (SR in H versus time) are shown on Fig. 7. They show that the loop performs with a rather stable behaviour and in equal ways when using TOMO and GLAO–mean modes, which is good as it shows that the tweeter allows to “get rid” of the action of the woofer stage. Conversely, what happens with the GLAO–ls is exactly what we do not want, as we experience a loss of 5 points on the SR. This is typically an

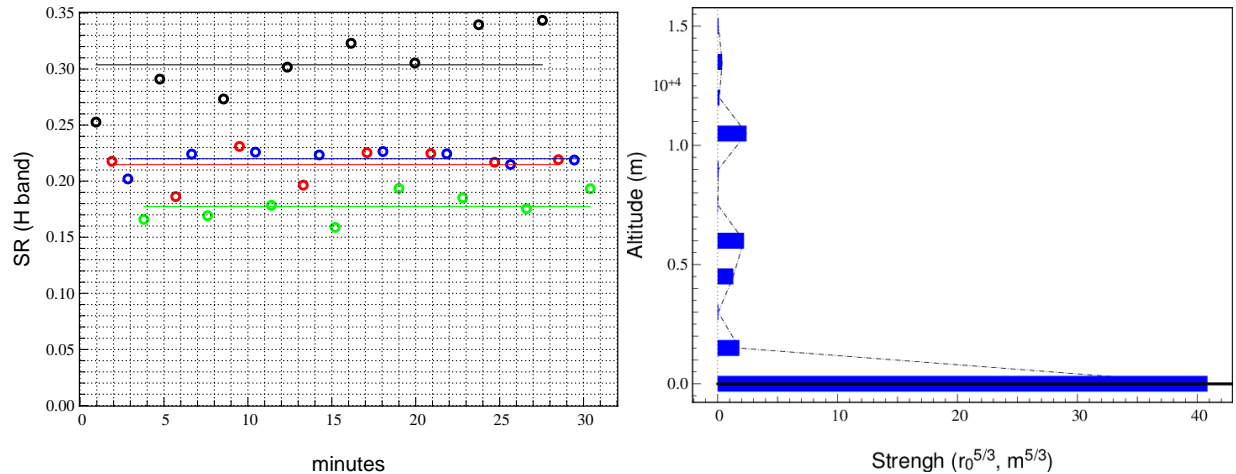


Figure 7. Strehl ratio (in H band) versus time in minutes. Black: SCAO using woofer and tweeter. Other modes use the same on-axis tomographic reconstructor on the tweeter, but either use TOMO (red), GLAO-mean (blue), GLAO-ls (green) on the woofer. The horizontal lines show the average value of the SR for each mode. Data from June 27-28 2015, script 36. Right: profile that was used in the tomographic reconstructor, retrieved by the L&A from previous data.

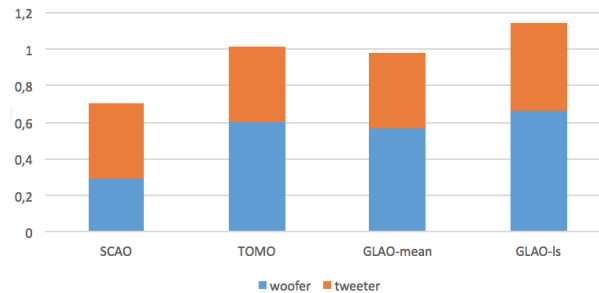


Figure 8. Median value of the rms fluctuation of the actuators of the two deformable mirrors (woofer in blue, tweeter in orange) for the 4 modes SCAO, TOMO, GLAO-mean and GLAO-ls, expressed in arbitrary units that make the 2 mirrors comparable. Tilt is excluded.

example where the command was badly designed, and we are introducing some modes on the woofer that cannot be “undo” with the tweeter. A more detailed analysis will be required here. But when looking at the required strokes each mirror has to employ in each mode (see Fig. 8), we find that the most economic one is SCAO, which is not surprising as both mirrors are working hand in hand. TOMO and GLAO-mean are strictly similar, but both require larger strokes than SCAO. The GLAO-ls exhibits larger strokes than any others, for both mirrors, showing that the woofer requires to adopt strange shapes (high order modes ?) that the tweeter needs to fight against.

One may wonder why the stroke required by the woofer in TOMO is higher than in SCAO. The reason is that the woofer TOMO stroke should be compared to the full stroke woofer+tweeter in SCAO, so that the TOMO stroke is actually a bit lower than in SCAO. GLAO-ls exhibits a larger stroke from both mirrors, the tweeter having to fight against the woofer.

### 6.5 Script example 3

In this script (script 24, night of June 30, 00:32 to 01:08) we varied the loop gain. In SCAO, this loop gain applies jointly on woofer and tweeter. In MOAO, the loop gain  $g$  was set to 0.1 on the woofer, and we only vary the gain  $g'$  on the tweeter. The behaviour is quite different in SCAO and MOAO. A long series of 32 files were acquired, with gains and observing modes interleaved in order to be able to properly average the data across seeing variations. The averaged results are shown on Fig. 9. The performance of the SCAO improves with the

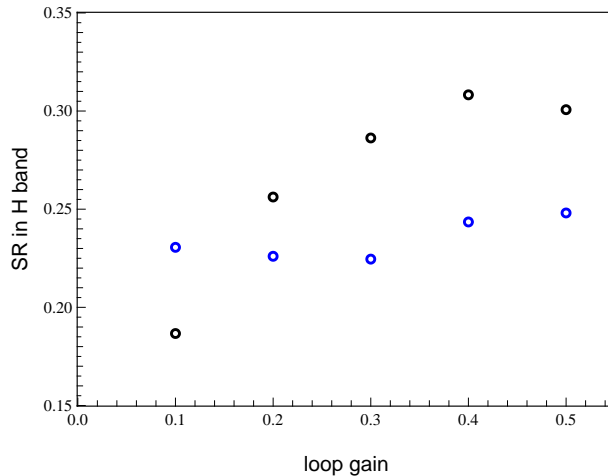


Figure 9. Strehl ratio in H band versus gain for SCAO (black) and MOAO (blue). While the impact of the gain is clearly visible in SCAO, the performance in MOAO is rather stable.

gain, up to  $g \approx 0.4$ , while the performance of MOAO remains rather flat. This has been observed regularly during our runs. The transfer functions are different between the two modes, the MOAO using a figure-locked mode on the tweeter. However a simulation is required to understand the detail.

## 7. CONCLUSIONS

In 2015, CANARY has successfully reached its final C2 phase, where the MOAO has been demonstrated on-sky using a 2-stage compensation scheme comparable to the E-ELT one.

Before that, CANARY has passed 3 important phases. Surprisingly, the less difficult was the LTAO (phase C1) one, as all the wave-front sensors in closed-loop allow easy calibrations while the efficiency of the close-loop scheme benefits to the performance.

Conversely, the difficulty of the step from C1 (LTAO) to C2 (2-stage MOAO) was the highest one, despite of our previous efforts and cumulated experience. The increase of sub-aperture count of 5 registered wave-front sensors was an underestimated challenge. The tomographic process combining wave-front sensors of inhomogeneous sub-aperture number was another one.

A supplementary challenge was the software. CANARY is not a regular instrument, observing using a few determined modes. It has been made to explore any possible configuration, any combination of any wave-front sensors, with any mode both on woofer and tweeter, producing data sets completed by the instrument configuration and associated to the web of dependencies towards calibration data they rely on. All of this comes with a backward compatibility with the previous phases, which make the software touchy.

Despite of the difficulty, CANARY has successfully produced its phase C2 data during the first observing night. However, a lot remains to be done in order to analyse those data. In particular the error budget on a 2-stage system has nothing to see with that of a single-DM system, and the analysis is difficult and is still ongoing today. The variability of on-sky conditions does not help this task. More detailed analysis will be made available in the coming months.

In 2016, CANARY will be reworked and will enter a new life, as a totally new experiment will take place, aiming at observing a 40 m off-axis sodium laser plume<sup>25</sup> and assessing the wave-front sensing performance on such a peculiar object. This phase will stop with the MOAO prospective. 2017 will also make a break in the life of CANARY, as the instrument WEAVE will be installed at the primary focus of the WHT telescope. It is however not excluded that CANARY could possibly come back to the telescope in 2018 for more MOAO, if the data analysis shows there is a strong particular need for it.

## 8. ACKNOWLEDGEMENTS

This work is supported by CNRS–INSU, Observatoire de Paris and Université Paris Diderot-Paris 7 in France, STFC and Durham University in UK and by European Commission (Fp7 Infrastructures 2012-1, OPTICON Grant 312430, WP1).

## REFERENCES

- [1] Cuby, J., Morris, S., Fusco, T., *et al.*, “EAGLE: a MOAO fed multi-IFU NIR workhorse for E-ELT,” in [*Ground-based and Airborne Instrumentation for Astronomy III*], *Proc. SPIE* **7735** (2010).
- [2] Gendron, E., Vidal, F., Brangier, M., *et al.*, “MOAO first on-sky demonstration with CANARY,” *Astron. & Astrophys.* **529**, L2 (2011).
- [3] Morris, T., Gendron, E., Basden, A., *et al.*, “CANARY Phase B: On-sky open-loop tomographic LGS AO results,” in [*Adaptive Optics Systems IV*], *Proc. SPIE* **9148** (2014).
- [4] Evans, C. J., Barbuy, B., Bonifacio, P., *et al.*, “Multi-object spectroscopy with the European ELT: scientific synergies between EAGLE and EVE,” in [*Ground-based and Airborne Instrumentation for Astronomy IV*], *Proc. SPIE* **8446** (2012).
- [5] Hammer, F., Barbuy, B., Cuby, J. G., *et al.*, “MOSAIC at the E-ELT: A multi-object spectrograph for astrophysics, IGM and cosmology,” in [*Ground-based and Airborne Instrumentation for Astronomy V*], *Proc. SPIE* **9147**, 914727 (2014).
- [6] Morris, T., Basden, A., Buey, T., *et al.*, “Adaptive optics for mosaics: design and performance of the wide(st)-field ao system for the e-elt,” in [*Adaptive Optics System V*], *Proc. SPIE* **9909**, to be published in these proceedings (2016).
- [7] Gratadour, D., Gendron, E., Grosset, L., *et al.*, “First demo science with MOAO: observations of distant merging galaxies with CANARY,” in [*Adaptive Optics Systems IV*], *Proc. SPIE* **9148** (2014).
- [8] Basden, A. G., Atkinson, D., Bharmal, N. A., *et al.*, “Experience with wavefront sensor and deformable mirror interfaces for wide-field adaptive optics systems,” *M.N.R.A.S.* **459**, 1350–1359 (2016).
- [9] Gach, J.-L., Feautrier, P., Balard, P., Guillaume, C., & Stadler, E., “OCAM2S: an integral shutter ultrafast and low noise wavefront sensor camera for laser guide stars adaptive optics systems,” in [*Adaptive Optics Systems IV*], *Proc. SPIE* **9148**, 914819 (2014).
- [10] Kellerer, A., Vidal, F., Gendron, E., *et al.*, “Deformable mirrors for open-loop adaptive optics,” in [*Adaptive Optics Systems III*], *Proc. SPIE* **8447** (2012).
- [11] Fusco, T., Sauvage, J.-F., Petit, C., *et al.*, “Final performance and lesson-learned of SAXO, the VLT-SPHERE extreme AO: from early design to on-sky results,” in [*Adaptive Optics Systems IV*], *Proc. SPIE* **9148**, 91481U (2014).
- [12] Charton, J., Bitenc, U., Curis, J.-F., *et al.*, “Recent improvements of high density magnetic deformable mirrors: faster, larger and stronger,” in [*Adaptive Optics Systems IV*], *Proc. SPIE* **9148**, 914825 (2014).
- [13] Bitenc, U., Bharmal, N. A., Morris, T. J., & Myers, R. M., “Assessing the stability of an ALPAO deformable mirror for feed-forward operation,” *Optics Express* **22**, 12438 (2014).
- [14] Gratadour, D., Gendron, E., & Rousset, G., “Practical issues with phase diversity for NCPA compensation resolved on the CANARY demonstrator,” in [*Proceedings of the Third AO4ELT Conference*], Esposito, S. & Fini, L., eds., 67 (2013).
- [15] Basden, A., Geng, D., Myers, R., & Younger, E., “Durham adaptive optics real-time controller,” *Appl. Opt.* **49**, 6354–6363 (2010).
- [16] Sivo, G., Kulesàr, C., Conan, J.-M., *et al.*, “First on-sky scao validation of full lqg control with vibration mitigation on the canary pathfinder,” *Optics Express* **22**, 23565–23591 (2014).
- [17] Basden, A. G., Myers, R. M., & Gendron, E., “Wavefront sensing with a brightest pixel selection algorithm,” *M.N.R.A.S.* **419**, 1628–1636 (2012).
- [18] Gilles, L. & Ellerbroek, B. L., “Split atmospheric tomography using laser and natural guide stars,” *Journal of the Optical Society of America A* **25**, 2427 (2008).

- [19] Tallon, M., Tallon-Bosc, I., Béchet, C., *et al.*, “Fractal iterative method for fast atmospheric tomography on extremely large telescopes,” in [*Adaptive Optics Systems II*], B. Ellerbroek, M. Hart, N. Hubin, P. Wizinowich, ed., *Proc. SPIE* **7736** (2010).
- [20] Vidal, F., Gendron, E., & Rousset, G., “Tomography approach for multi-object adaptive optics,” *JOSA A* **27**, A253–A264 (2010).
- [21] Vidal, F., Gendron, E., Rousset, G., *et al.*, “Analysis of on-sky MOAO performance of CANARY using natural guide stars,” *Astron. & Astrophys.* **569** (2014).
- [22] Martin, O., Gendron, E., Rousset, G., & Vidal, F., “Temporal convergence of phase spatial covariance matrix measurements in tomographic adaptive optics,” in [*Adaptive Optics Systems III*], *Proc. SPIE* **8447**, 84472A–1 (2012).
- [23] Gendron, E., Charara, A., Abdelfattah, A., *et al.*, “A novel fast and accurate pseudo-analytical simulation approach for MOAO,” in [*Adaptive Optics Systems IV*], *Proc. SPIE* **9148** (2014).
- [24] Gendron, E., Morel, C., Osborn, J., *et al.*, “Robustness of tomographic reconstructors versus real atmospheric profiles in the ELT perspective,” in [*Adaptive Optics Systems IV*], *Proc. SPIE* **9148** (2014).
- [25] Rousset, G., Gratadour, D., Gendron, E., *et al.*, “Proposal for a field experiment of elongated Na LGS wave-front sensing in the perspective of the E-ELT,” in [*Adaptive Optics Systems IV*], *Proc. SPIE* **9148** (2014).